MATERIALS CHEMISTRY
FRONTIERS

CCS 中国化学会 CHINESE CHEMICAL SOCIETY
ICCAS
ROYAL SOCIETY OF CHEMISTRY

RESEARCH ARTICLE

View Article Online
View Journal | View Issue

Cite this: *Mater. Chem. Front.*, 2023, **7**, 753

Green synthesis of 3D cesium lead halide perovskite nanocrystals and 2D Ruddlesden–Popper nanoplatelets in menthol-based deep eutectic solvents†

Shovon Chatterjee, Arghya Sen and Pratik Sen *

Received 18th November 2022,
Accepted 18th January 2023

DOI: 10.1039/d2qm01188c

rsc.li/frontiers-materials

Organic solvent hazards are the most overlooked part of perovskite research. In this report, we employed menthol based deep eutectic solvents (DESs) as a green medium for the synthesis of cesium lead halide ($CsPbX_3$; X = Cl, Br, I, or either both) nanocrystals (NCs) and nanoplates (NPLs) with high PLQY (maximum of 78%) aiming to reduce the synthesis related toxicity. The reaction temperature and added precursor ratio in the DES medium were found to be the key factor in controlling the dimensionality of the NCs. The synthesized NCs and NPLs in the DES medium suffer from common halide vacancy-related defects, which were passivated by oleylammonium halide treatment to achieve near unity PLQY. With green DES as a synthesis medium, the present synthetic protocol lowered the crystallization temperature, allowing ambient condition synthesis, and yields high quality NCs/NPLs with an almost uniform size distribution. This study presents a novel approach to the environmentally friendly synthesis of NCs and NPLs, which holds great potential for the practical large-scale synthesis of perovskites in industrial settings.

Introduction

Nature necessitates the environmental sustainability of all industrial productions. Among several factors, solvent use is a substantial contributor to the overall toxicity profile of an industrial process.[1,2] To tackle this issue, diverse green solvents are being introduced in lieu of conventional hazardous organic solvents in a variety of applications.[2–4] Amidst all the alternate solvent media, deep eutectic solvents (DESs) are quickly gaining interest among researchers because of their uniqueness like easy preparation, fine tunability, cost-effectiveness, *etc.*[3–5] Although DESs have already been identified as alternate solvents for biochemical applications,[4,5] their use in materials science has not been explored yet. Herein, we used menthol-based DESs as a green solvent media to synthesize pure inorganic cesium lead halide nanocrystals (NC) ($CsPbX_3$ NCs, X = Cl, Br, I) which largely reduces the organic solvent-related hazards of perovskite NC synthesis. The photoluminescence tunability from violet to red has been achieved in DES media by tuning the halide compositions. The reaction temperature and cesium to lead precursor ratio in the DES medium were found to be the key factor in controlling the dimensionality and were further used to synthesize Ruddlesden–Popper $(OAm)_2Cs_2Pb_3Br_{10}$ nanoplatelets (NPLs) with blue photoluminescence.

Perovskite research has advanced at breakneck speed in the last decade.[6,7] Due to their defect-tolerant nature, high photoluminescence quantum yield (PLQY), and narrow PL bandwidth, the nanocrystalline form of lead halide perovskites have proved their immense potential in the field of opto-electronics.[6,7] However, because of their low environmental and water stability, their practical application is still a long way off.[8,9] Lead toxicity is still a key issue in perovskites, which is driving the development of lead-free perovskites.[10,11] However, overcoming solvent-related toxicity during synthesis (typically due to toxic DMF, NMP, skin penetrating DMSO, skin irritant octadecene, *etc.*) is yet another crucial but overlooked aspect of this research field.[12] Another major worry is that these precursor solvents have a high propensity to coordinate with the perovskite surface, allowing the perovskite structure to degrade.[13] Using ionic liquids (ILs) as a precursor media, a few breakthroughs have been achieved in this direction.[12] Moore *et al.* reported the synthesis of methylammonium lead iodide thin films from a methylamine/short chain carboxylic acid IL medium in 2015.[14] Following this, a number of studies have been published that indicate how IL additives can regulate crystal formation, stability, and surface modification in

Department of Chemistry, Indian Institute of Technology Kanpur, Kanpur – 208 016, UP, India. E-mail: psen@iitk.ac.in; Fax: +91 512 259 6806; Tel: +91 512 259 6312

† Electronic supplementary information (ESI) available: Supporting information includes PXRD analysis, XPS analysis, TEM analysis, and all related supporting tables. See DOI: https://doi.org/10.1039/d2qm01188c

perovskite thin films.[12,15] However, all of these reports revolve around the thin film/solar cell applications of perovskites. For the first time Hoang *et al.* reported the green synthesis of methylammonium lead bromide NCs in 2020.[16] By combining methylamine with short-chain aliphatic carboxylic acids, they were able to synthesize an IL medium, which was used to synthesize $MAPbBr_3$ NCs with ~50% PLQY. Recently, we employed highly hydrophobic lauric acid to prepare a methylammonium laurate IL medium, which finally leads to the formation of water stable $MAPbBr_3$@laed laurate core–shell nanostructure with near-unity PLQY.[17]

One of the major drawback of this IL-based alternate solvent media is the poor solubility of the precursor salts. The use of solid lead halide salts for synthesizing perovskites in IL media restricts the possibility of the doping and synthesis of mixed perovskite materials.[16,17] The only solution is to increase a universality of the alternate solvent, where both the hydrophobic and hydrophilic precursors are soluble. To tackle this issue we have used menthol based DESs (Fig. 1a–d), *ca.* 1 : 2 lauric acid/menthol (LAMe), 1 : 1 caprylic acid/menthol (CAMe), and 1 : 1 butyric acid/menthol (BAMe).[18,19] The solubility of lead halide salts in these DES media are excellent in the presence of oleylamine (OAm). Using this key solubility factor, we have synthesized highly luminescent $CsPbX_3$ NCs and 2D RP NPLs in this green DES medium.

Experimental section

Chemicals

Menthol (Sigma Aldrich, 99%), lauric acid, caprylic acid, butyric acid, lead bromide (Sigma Aldrich, 99%), lead chloride (Sigma Aldrich, 99%), lead iodide (Sigma Aldrich, 99%), and oleylamine (TCI Chemicals, 60%) were used as received. Hydrochloric acid (Merck, 37% in water), hydrobromic acid (Alfa-Aesar, 48% water), hydroiodic acid (TCI, 57% in water), and hexane (TCI) were used without further purification.

Synthesis of DESs

The DESs were synthesized by heating acids in the right molar ratio with menthol. LA-menthol DES (LAMe) is created by mixing LA with menthol in a 1 : 2 ratio. CA-Menthol (CAMe)

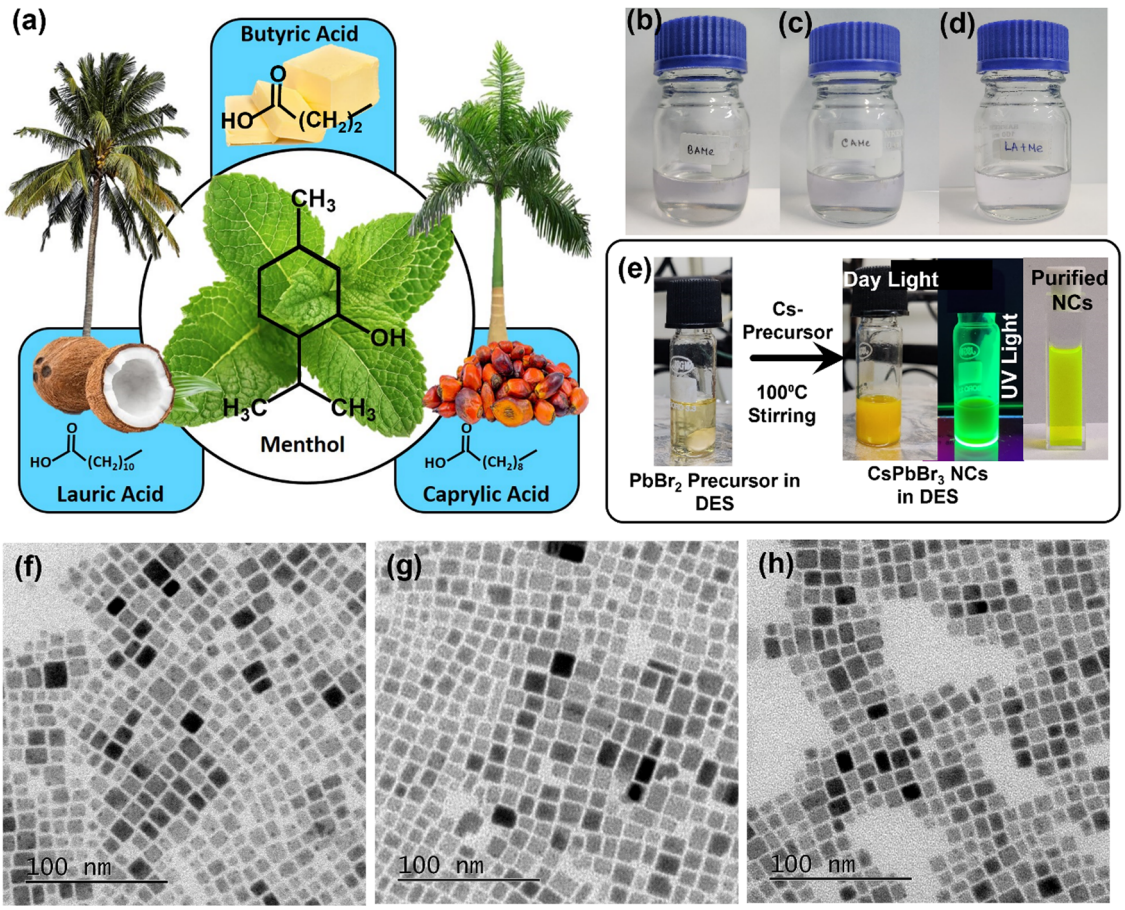

Fig. 1 DES as a synthesizing medium. (a) Natural sources of the menthol, lauric acid (LA), caprylic acid (CA) and butyric acid (BA). Photographic images of (b) BAMe, (c) CAMe and (d) LAMe deep eutectic solvents. (e) Preparation of $CsPbBr_3$ NCs in a DES medium. Photographic image of crude $CsPbBr_3$ NCs in day light and under UV light is also given. A photographic image of a purified NC suspension is given in the right most side. Transmission electron microscopic (TEM) images of (f) $CsPbBr_3$ NCs in a LAMe DES medium (CPB-LAMe), (g) $CsPbBr_3$ NCs in a CAMe DES medium (CPB-CAMe), and (h) $CsPbBr_3$ NCs in a BAMe DES medium (CPB-BAMe).

and BA-Menthol DESs, on the other hand, were created in a 1 : 1 ratio using the same process. The DESs are transparent liquids at room temperature. These DESs were characterized using FTIR, and thermogravimetric studies (TGA).

H-bond donor (HBD)	H-bond acceptor (HBA)	Molar ratio	Appearance
Lauric acid (LA)	Menthol	1 : 2	Transparent liquid
Caprylic acid (CA)	Menthol	1 : 1	Transparent liquid
Butyric acid (BA)	Menthol	1 : 1	Transparent liquid

Synthesis of Cs-precursor in DES medium

0.69 g of $CsCO_3$ salt was added to 1 ml of DES (LAMe, CAMe or BAMe) and was stirred at 100 °C until it formed a clear colourless solution. This Cs-precursor was stored in normal atmospheric conditions. At room temperature this Cs-precursor become solid. This was again re heated at different temperatures (depending upon the NC synthesizing temperature) before injecting.

Synthesis of oleylammonium bromide (OAmBr) and oleylammonium iodide (OAmBr) salts

OAmX salts were prepared by the procedure reported in our previous publication.[17] In short, 10 ml of oleylamine (OAm) was taken along with the required amount of hydrohalic acid (For OAmBr 1.28 mL of HBr and for OAmI 1.5 mL of HI) in a 25 mL two-neck round-bottomed flask. The resulting reaction mixture was heated at 120 °C for 2 h in a nitrogen atmosphere. The reaction temperature was then increased to 150 °C and the mixture was further heated for 30 min. The concentrations of the OAmBr and OAmI salts were 1.07 mmol mL^{-1} and 1.14 mmol mL^{-1}, respectively. The hexane diluted solution (0.051 mmol mL^{-1} OAmBr) was then used for surface treatments.

Synthesis of $CsPbBr_3$ NCs in DES medium

7.2 mg of $PbBr_2$ salt was placed in a vial with 2 ml DES (LAMe, CAMe or BAMe). Then 150 μL of OAm was added to this mixture and stirred at 100 °C until $PbBr_2$ fully dissolved. The cesium precursor was then heated at 100 °C. 100 μL of this heated cesium precursor was then swiftly injected into the $PbBr_2$ precursor in the DES. Instantly light yellow colored NCs formed which showed green photoluminescence under UV light. These NCs were then centrifuged at 15 000 rpm for 1 hour. The supernatant DES was discarded and the NCs were washed thoroughly with methyl acetate and were then dissolved in hexane and centrifuged again at 10 000 rpm for 10 mins. The residue, containing the large particles, was discarded. The supernatant contained NCs of uniform size and was used for further studies.

$CsPbBr_3$ NPLs with different width were synthesized using the same procedure, except for changing the temperature (100 °C, 75 °C, and 50 °C) and the cesium precursor amount (25 μL, 50 μL, 75 μL and 100 μL) in LAMe.

It is important to mention that, we were not able to synthesize stable $CsPbI_3$ NCs by using the OAm ligand. The synthesized $CsPbI_3$ using the OAm ligand quickly transferred to the non-emissive yellow phase immediately after preparation. For this, we have alternatively used an OAmI salt as a ligand to synthesize relatively stable $CsPbI_3$ NCs.

Synthesis of other $CsPbX_3$ NCs (X = Cl, Cl/Br, Br/I, and I) in DES medium

The other halide perovskite NCs were also prepared by a similar procedure except for $CsPbI_3$ NCs. For $CsPbCl_3$ NCs, 5.4 mg of $PbCl_2$ salt was dissolved in 2 ml LAMe DES in the presence of OAm at 100 °C. Then 100 μL of the Cs-precursor was injected into it. Immediately a white colour of $CsPbCl_3$ NC formed. These NCs were then centrifuged at 15 000 rpm for 1 hour. The supernatant DES was discarded and the NCs were dissolved in hexane and centrifuged again at 10 000 rpm for 10 mins. The supernatant contained NCs of uniform size and were used for further studies. For $CsPb(Cl/Br)_3$, a mixture of 2.7 mg of $PbCl_2$ and 3.6 mg of $PbBr_2$ were taken in DES whereas for $CsPb(Br/I)_3$ NCs 3.6 mg of $PbBr_2$ and PbI_2 were taken and the respective NCs were prepared by a similar procedure. For $CsPbI_3$ NCs, 9 mg of PbI_2 was dissolved in 2 ml LAMe in the presence of 200 μL OAmI and was then prepared by similar procedure.

In the present study DESs are used as the solvent media for the synthesis of perovskites. We believe the formation of cesium carboxylate through the reaction between Cs_2CO_3 and RCOOH (a DES component) is the primary step for the reaction that then combines with PbX_2 to form $CsPbX_3$ (where X is Cl, Br, I), as shown below.

$$Cs_2CO_3 + RCOOH = 2CsCOOR + H_2O + CO_2$$

$$2CsCOOR + 3PbX_2 = 2CsPbX_3 + Pb(COOR)_2$$

Surface treatment of CPB NCs/NPLs with OAmBr

The surface treatment by OAmBr salt was done by a dilute solution of OAmBr in hexane (0.051 mmol ml^{-1}). 20μL of this diluted solution was added to the hexane suspension of CPB-LAMe having an absorbance of 0.21 at the absorption band edge. For CPB-2D (n = 3), again 20 μL of this diluted solution of OAmBr was added to the NPL suspension having an absorbance of 0.25 at the excitonic band edge maxima.

Synthesis of $CsPbBr_3$ NCs by a hot injection procedure (pristine CPB)

The pristine $CsPbBr_3$ NCs were prepared by the reported procedure by Protesescu *et al.*[20] In brief, 0.16 g of Cs_2CO_3, 6 mL of ODE, and 0.5 mL of OA were mixed together in a 50 mL double-necked round-bottom flask (RB), which was heated under vacuum at 120 °C for an hour and then under nitrogen

atmosphere until all of the Cs_2CO_3 had reacted with OA to form Cs-oleate. This solution was maintained at this temperature for its use to avoid precipitation. In another 50 mL double-necked RB, 0.069 g of $PbBr_2$ along with 5 mL of ODE, 0.5 mL of OA, and 0.5 mL of OAm were mixed and heated under vacuum at 110 °C for an hour. The temperature was then increased to 170 °C under a nitrogen atmosphere and 0.45 mL of pre-heated Cs-oleate solution was injected swiftly followed by immediate cooling of the solution in ice-cold water. The NCs were obtained by collecting the precipitate upon centrifuging the whole dispersion at ~8000 rpm and were washed with 1:1 methyl acetate followed by dispersing in hexane for further measurements.

Microscopic characterizations

The high-resolution transmission electron microscopic (HRTEM) images were collected on a Titan G^2 60-300 microscope. Samples for HRTEM were prepared by casting one drop of the diluted suspension of NCs after 10 mins of sonication on a carbon-coated copper grid (Ted Pella). The grid was dried overnight before imaging.

Powder X-ray diffraction (PXRD)

X-ray diffraction patterns were collected by a PANalytical Xpert Powder diffractometer with Cu-Kα as the incident radiation (λ = 0.154 nm) in the 2θ range between 5° to 50° with steps of 0.01°. For the sample preparation, we have used an NC suspension in hexane. This NC dispersion was then drop casted on a glass slide and kept in the open air for complete solvent evaporation.

X-Ray photoelectron spectroscopy (XPS)

The XPS data were collected using a PHI 5000 Versa Prob II instrument. The sample was prepared by same process as for powder XRD on a very thin glass slide.

IR measurements

The Fourier transform infrared (FTIR) measurements were carried out using a Bruker Alpha-P FTIR with an ATR accessory.

TGA measurements

The thermal stabilities of the DESs were determined by thermogravimetric analysis (TGA) using a Mettler Toledo TGA/DSC 1 instrument. A dynamic mode at a temperature range from (17 to 250) °C with a heating rate of 5 °C min^{-1} was used to determine the onset of decomposition temperatures.

Absorption, emission and PL-lifetime measurements

The absorption and emission spectra were collected in a commercial UV−visible spectrophotometer (UV-2450, Shimadzu, Japan) and spectrofluorimeter (FluoroMax4, Jobin-Yvon, USA), respectively. The PL transients were recorded using a commercial time correlated single photon counting (TCSPC) setup (LifeSpecII, Edinburgh Instruments, UK) with excitation by a 405 nm diode laser (EPL-405, Edinburgh Instruments, UK) at the magic angle condition. The full width at half maxima of the instrument response function (IRF) was 120 ps. The average lifetimes were calculated using the following equation:

$$\tau_{avg} = \sum_i \frac{a_i \tau_i^2}{a_i \tau_i} \quad (1)$$

Where τ_i is the lifetime of the i-th component and a_i is the relative percentage of the i-th lifetime component. The PL transients were fitted with the sum of two exponentials along with the deconvolution with the IRF. The PL quantum yield (PLQY) of the NCs was calculated using coumarin 30 in acetonitrile as the reference.

Femtosecond transient absorption spectroscopy study

Transient absorption spectra were recorded in our broadband femtosecond transient absorption spectrometer (Femto-Frame-II, IB Photonics, Bulgaria). The fundamental output 800 nm 80 fs beam from a Ti-Sapphire regenerative amplifier (SpitfirePro XP, Spectra-Physics, USA) pumped by a 20 W Q-switched Nd:YLF laser (Empower, Spectra-Physics, USA) and seeded by a Ti-Sapphire femtosecond oscillator (MaiTai SP, Spectra-Physics, USA) was divided into two parts. One portion was passed through a β-barium borate crystal to generate the second harmonic light (400 nm). The other part was focused onto a sapphire crystal to generate the white light continuum after passing through a retro-reflector to adjust the delay between the pump and probe light. The 400 nm light is the pump and the white light continuum spread over 450–750 nm is the probe in our setup. The maximum delay of 1 ns is recorded in the setup for this experiment. The pump and probe light are focused on a 1 mm cuvette containing the sample and after passing through the sample, and only the probe light was collected, dispersed in polychromator and detected using a CCD detector. The pump power is generally kept 5 μW and the probe power was kept much less than the pump power. The overall instrument response function was 120 fs.

Result and discussion

The DESs have excellent heat tolerance and remain colourless liquids at room temperature. The TGA study shows no weight loss until 100 °C for LAMe and CAMe (see Fig. S1 of the ESI†). However, the degradation of BAMe starts around 60 °C (see Fig. S1 of the ESI†). IR measurements were performed to characterize the DES media as well. Menthol has a broad O–H frequency centered at 3453 cm^{-1}, and all acids are characterized by a carbonyl frequency of ~1700 cm^{-1}. Both of the peaks get modified following the preparation of the DES (see Fig. S2 of the ESI†). The formation of a hydrogen bonding network between menthol and different acids is indicated by such alterations in the carboxylic carbonyl stretching frequency to higher values. The shift is most noticeable in LAMe, implying the highest hydrogen bonding interaction among the three DESs.

Among the pure inorganic perovskite NCs, green-emitting $CsPbBr_3$ is the most celebrated considering its structural

stability and massive PLQY. The major synthetic protocol for the synthesis of this NC is the hot injection method, where the temperature is raised to ~170 °C in inert atmospheric conditions to initiate the crystallization. Also in the hot injection procedure, there is still no replacement of the hazardous and toxic octadecene solvent. By keeping these drawbacks in our mind, we planned to introduce a green solvent where a comparatively lower injection temperature is used for the crystallization of NCs without any inert atmospheric conditions. $CsPbBr_3$ NC was synthesized by a simple two-precursor approach at 100 °C in open atmospheric conditions by utilizing the above mentioned DES media (see Fig. 1e and the Experimental section). The $CsPbBr_3$ NCs synthesized in LAMe, CAMe and BAMe are named as CPB-LAMe, CPB-CAMe, and CPB-BAMe, respectively. The powder XRD patterns confirm that the formed NCs are in a pure cubic crystalline phase (Fig. S3 of the ESI†). The FTIR spectra are utilized to probe the capping ligand environments of purified dry CPB-LAMe, CPB-CAMe, and CPB-BAMe NCs which are shown in Fig. S4 of the ESI.† All of the NCs have a weak and broad absorption band near 3400 cm^{-1}, which originates from N–H stretching and absorptions at ~2900 cm^{-1} and 1460 cm^{-1} are a characteristic signature of the C–H stretching and bending mode respectively due to the OAm capping ligand. The presence of the corresponding aliphatic acids from the DESs as a capping ligand on the NC surface is indicated by another distinctive absorption band at 1700 cm^{-1} in all cases. Therefore, we can clearly conclude that all of the synthesized CPB NCs have X-type OAm and alkyl carboxylic acid (a constituent of DES) capping ligands on the NC surface.[6,21] An energy dispersive X-ray (EDS) analysis of the NCs was carried out to have an idea about the elemental ratios of the NCs. CPB-LAMe shows a bromine to lead ratio of 2.76 : 1, while for CPB-CAMe and CPB-BAMe it is 2.54 : 1 and 2.44 : 1, respectively, suggesting a bromine deficient surface in all three NCs (Fig. S5 of the ESI†). This may originate from the bromine-deficient reaction conditions as $PbBr_2$ salt was utilized as a dual source of bromine and lead in our synthesis. This problem is quite common in hot injection synthetic processes.[22,23] The X-ray photoelectron spectroscopy of CPB-LAMe was carried out to have a better understanding of the surface composition of the NCs. The XPS analysis reveals that the surface of CPB-LAMe has a bromine to lead ratio of 2.81 (Fig. S6 of the ESI†). The high resolution XPS spectra further reveal the formation of Pb^0 along with the CPB NCs (Fig. S6 of the ESI†). The appearance of Pb^0 may be because of the mild reducing power of OAm.[24]

Fig. 1f–h show the transmission electron microscopic (TEM) images of CPB-LAMe, CPB-CAMe, and CPB-BAMe, respectively. In all cases, we can see the formation of almost square-shaped NCs with uniform size distribution. The average size of CPB-LAMe is found to be 12 ± 3.6 nm whereas the average size of CPB-CAMe and CPB-BAMe are found to be 12 ± 4 nm and 11.2 ± 3.4 nm respectively (Fig. S7 of the ESI†). The ring pattern in the SAED confirm the cubic polycrystalline nature of the synthesized NCs (Fig. S8 of the ESI†) for all cases. Fig. S9a of the ESI† shows the HRTEM image of the CPB-LAMe. Fourier filtration of the selected area from Fig. S9d (ESI†) clearly shows two crystal planes (110) and (200) corresponding to interplanar distances of 0.41 nm and 0.29 nm respectively. Fig. S9b and S9c (ESI†) shows the HRTEM images of CPB-CAMe and CPB-BAMe respectively. Two crystal planes (110) and (200) corresponding to interplanar distances of 0.40 nm and 0.30 nm, respectively, can be seen from the Fourier filtration from the selected area (Fig. S9 of the ESI†). For CPB-BAMe similarly, two crystal planes (100) and (110) can be visualized from the Fourier filtered image as well (see Fig. S9f of the ESI†). Therefore, we conclude that our green solvent mediated lower temperature synthesis in open atmospheric conditions is capable of producing high quality CPB NCs with a uniform size distribution.

The CPB NCs prepared in three different DES media at identical conditions (100 °C) show almost identical optical properties. The NCs show a broad absorption with an absorption edge at 510 nm and a sharp PL band centered at 513 nm in all cases (Fig. 2). However, CPB-LAMe exhibited a high PLQY of 78%, whereas the NCs prepared in CAMe and BAMe show relatively lower PLQY of 67% and 65%, respectively. The reason for a high PLQY of $CsPbBr_3$ NCs prepared in LAMe may be because of the effective passivation of the CPB NC surface by both OAm and LA. To gain insight into the charge carrier dynamics, the time-resolved PL studies of all three purified CPB NCs have been done. All the time-resolved PL data have been fitted with a sum of three exponential fitting functions, suggesting three different recombination sites present in the NCs. All the fitting parameters are tabulated in Table S1 of the ESI.† The long lifetime component of ~20 ns is assigned to the recombination of the charge carriers through the surface trap states.[24,25] The ~6 ns lifetime component is ascribed to the excitonic recombination process. [24–26] Although in some literature, an opposite assignment has been proposed for the shorter and longer lifetime components.[27,28] In a recent article, Becker *et al.* proposed that the long lifetime component originates from the trap induced delayed fluorescence.[29] Thus, the assignments of these two lifetime components are still under debate and need further detailed investigation. The origin of the shortest component ~1.4 ns is also a little bit ambiguous. The literature says that this component indicates the presence of additional defect sites in the NCs that facilitate the non-radiative processes.[22] This means that the CPB NCs can have trapping sites other than the trap states that originate from the unsaturated surface dangling nonbonding orbitals. One possibility of such a trap state is the bromine vacancy in the NCs. To verify this, we treated the NC suspension with a hexane solution of OAmBr that acts as a source of bromide ions. This post-synthetic treatment amplifies the PLQY of the system to near unity from 78% and increases the average lifetime from 13.1 ns to 14.9 ns, suggesting a suppression of nonradiative decay channels in the system. Interestingly, the short lifetime component of 1.4 ns disappeared after OAmBr treatment (see Table S2 of the ESI†). This further suggests the origin of the short lifetime component is the recombination of the charged carrier through bromine-related trap states. The PL stability of these colloidal NCs was monitored for two months in ambient

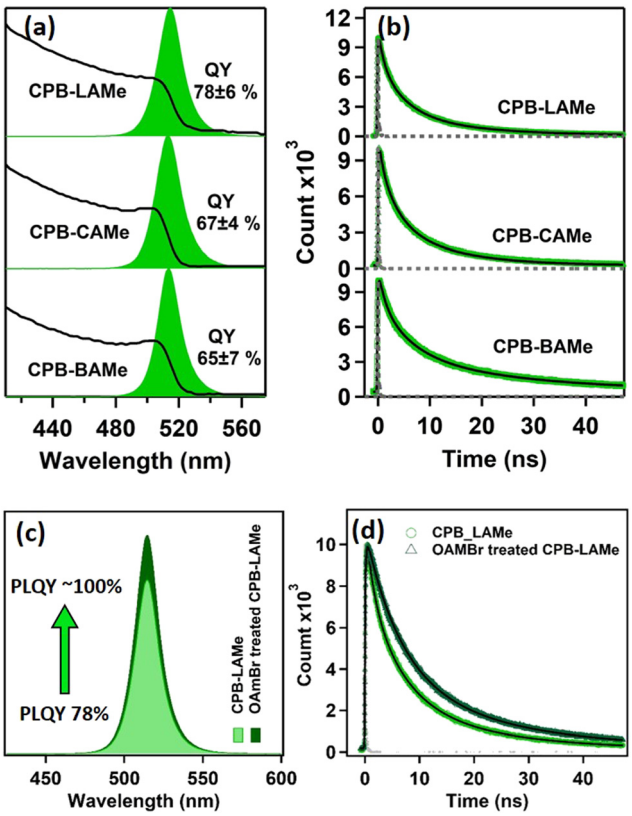

Fig. 2 Optical properties of $CsPbBr_3$ NCs synthesized in a DES medium (CPB NCs). (a) Steady state absorption (black spectrum) and PL (green solid spectrum) of hexane dispersed $CsPbBr_3$ NCs synthesized in a LAMe DES medium (CPB-LAMe) (top panel), $CsPbBr_3$ NCs synthesized in a CAMe DES medium (CPB-CAMe) (middle panel), and $CsPbBr_3$ NCs synthesized in a BAMe DES medium (CPB-BAMe) (lower panel). Corresponding PLQY values are given alongside. (b) Time resolved PL of a hexane suspension of CPB-LAMe (top panel), CPB-CAMe (middle panel) and CPB-BAMe (lower panel). (c) PL amplification from PLQY 78% to near unity upon OAmBr treatment on CPB-LAMe. (d) Corresponding increment in PL lifetime after OAmBr treatment on CPB-LAMe. The excitation source was a 405 nm laser having IRF 120 ps for all PL transient measurements.

conditions. CPB-LAMe was found to retain ~84% of its original PL intensity after two months. Whereas CPB-CAMe and CPB-BAMe retained ~60% of their PL intensity (see Fig. S10 of the ESI†). This may be due to the better capping environment of CPB-LAMe, which restricts its PL intensity loss in ambient conditions.

To have a better insight on the charge carrier dynamics of the synthesized CPB-LAMe, femtosecond transient absorption spectroscopic measurements were performed, and the results are compared with the pristine $CsPbBr_3$ NCs prepared through the frequently followed hot injection procedure (pristine CPB) (see Fig. S11 and S12 of the ESI† for TEM and optical characterizations, respectively). The samples were excited above the band gap at 400 nm with a femtosecond pulsed laser by maintaining the same excitation power, and the time-resolved difference absorption was measured. The results are shown in Fig. 3. CPB-LAMe and pristine CPB shows strong photobleach signals (PB) at 512 nm and at 507 nm, respectively, which correspond to their ground state bleaching (GSB). At early times a strong excited state absorption (ESA) band around 530 nm is observed for both the NCs corresponding to the hot carrier (HC) absorption.[30] For both CPB-LAMe and pristine CPB NCs, the kinetics were fitted with a sum of three exponential functions. The transient at the PB maxima (512 nm) shows a rise time component of 270 fs (Fig. 3d) that corresponds to the cooling of the HCs to the band edge position.[30,31] For pristine CPB, the HC cooling process shows a lifetime of 510 fs (Fig. 3f), which is in line with previous studies.[30] The relaxation of hot carriers to the band edge depends on the carrier-phonon coupling.[32,33] The HC relaxation becomes faster when the carrier-phonon interaction is higher.[32,33] This carrier-phonon interaction in a particular NC is highly dependent on the size of the NCs and also on the ligand environment under the same excitation fluence.[27,34] An earlier study shows that the HC cooling rate becomes dramatically slower if the NC size is reduced.[34] The pristine CPB NCs have an average edge length of 8 nm, which is smaller than the CPB-LAMe NCs (average edge length of 12 nm). As, the ligand environment is similar for both CPB-LAMe and pristine CPB NCs, the smaller size of pristine CPB than CPB-LAMe may be the reason for the slower HC cooling rate. Both CPB-LAMe and pristine CPB NCs show comparable two-component decay kinetics. The faster time constant of ~70 ps is assigned as a biexciton lifetime and the longer component (>1 ns) is assigned as an excitonic recombination process according to the literature.[25] The relative contribution of the biexcitonic species in CPB-LAMe and in pristine CPB remains almost similar in the same experimental conditions.

The reaction temperature in perovskite NC synthesis typically plays a pivotal role to determine the size, morphology, and properties of the synthesized NCs.[35,36] In the common hot injection process, tuning the reaction temperature is still a key in tuning the size of the synthesized NCs. Apart from the temperature, the ratio of the reactant salts is also a paramount factor that can influence the NC properties to a certain extent.[37] To see the effect of these two important factors in the perovskite NC synthesis in the DES media, we have studied the effect of reaction temperature and Cs:Pb precursor ratio on the properties of the prepared CPB NCs. Fig. 4a–c shows the absorption and PL properties of the NCs prepared in LAMe DES at three different temperatures (100 °C, 75 °C, and 50 °C) and four different precursor ratios. The ratio of precursors has no effect on the optical properties of the NCs if the reaction temperature is 100 °C. In all cases, the NCs show a strong PL at 513 nm with a broad absorption, which resembles 3D NCs ($n = \infty$) (Fig. 4a). At 75 °C reaction temperature, the PL properties of the NCs changes drastically depending on the precursor ratio. For all cases the multipeak PL bands were observed (Fig. 4b). The absorption bands also show similar sharp excitonic features in accordance with the PL. This observation suggests the formation of lower-order perovskite NPLs (Fig. 4b). The PL shows sharp maxima at ~460 nm, ~470 nm, ~480 nm, and 513 nm, which are assigned to NPLs with n = 3,4,5 and ∞ respectively. Here, n denotes the number of

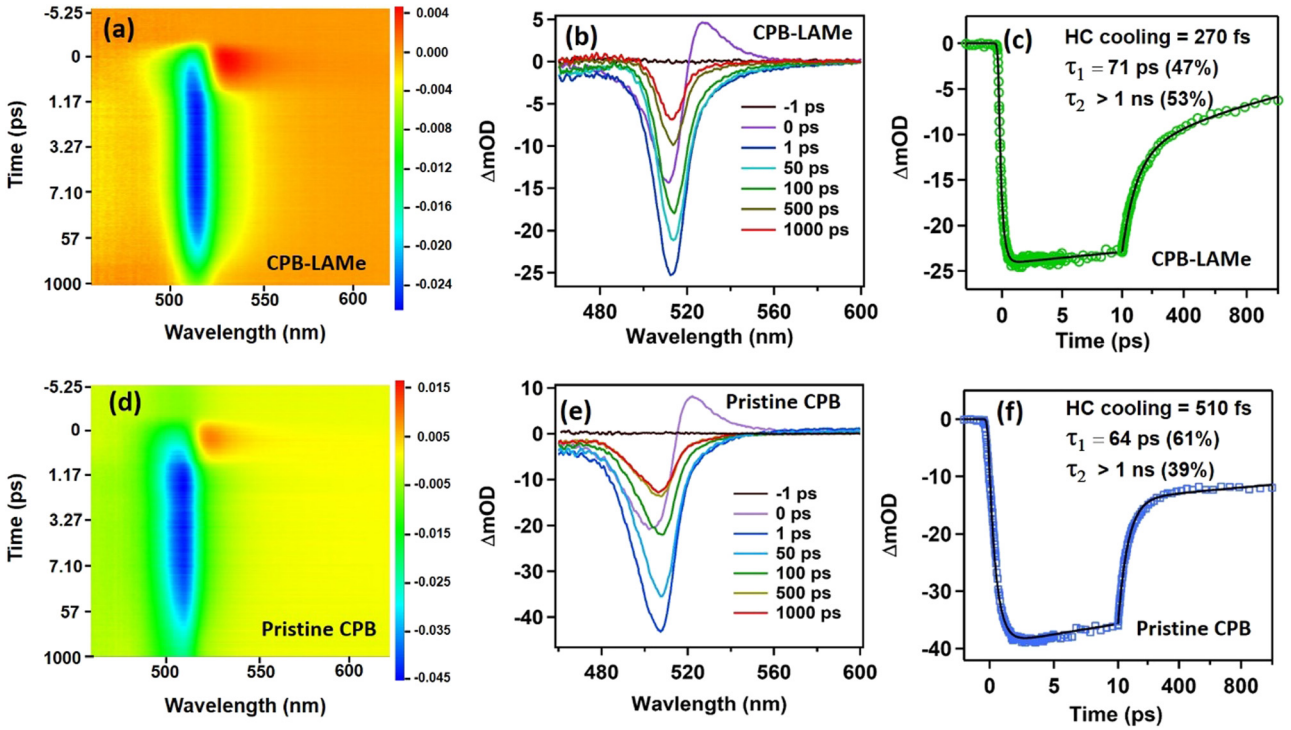

Fig. 3 Ultrafast carrier dynamics of $CsPbBr_3$ NCs synthesized in a LAMe DES medium (CPB-LAMe) and pristine CPB. (a) Two-dimensional pseudo color mappings of the TA spectra of $CsPbBr_3$ NCs synthesized in a LAMe DES medium (CPB-LAMe). (b) Representative TA spectra of $CsPbBr_3$ NCs synthesized in a LAMe DES medium (CPB-LAMe) at different times. (c) 512 nm transient of $CsPbBr_3$ NCs synthesized in a LAMe DES medium (CPB-LAMe). (d) Two-dimensional pseudo color mappings of the TA spectra of pristine $CsPbBr_3$ NCs (pristine CPB). (e) Representative TA spectra of pristine $CsPbBr_3$ NCs (pristine CPB) at different times. (f) 507 nm transient of pristine $CsPbBr_3$ NCs (pristine CPB).

$PbBr_6^{4-}$ octahedral layers in the NPLs.[38,39] The intensity ratios of the PL peaks vary with the cesium to lead ratio suggesting a change in the value of n. The TEM images of the sample prepared at 75 °C with unit cesium to lead ratio indicates the formation of different NPLs with 3D NCs (Fig. S13 of the ESI†). By lowering the reaction temperature to 50 °C and by using a cesium to lead ratio of 0.25 we were able to synthesize a pure NPL (n = 3) having a sharp excitonic absorption peak at 455 nm and a PL band centered at 460 nm (Fig. 4c and Fig. 5a). The overall effect of temperature and Cs:Pb precursor ratio are schematically shown in Fig. 4d. For a better understanding of the structure and properties, we proceed with this pure NPL (n = 3) for further characterization.

The PLQY of this NPL (n = 3) is measured to be 46%. The time-resolved PL decay profile of the colloidal CPB-2D (n = 3) can be best fitted using a sum of three exponential functions (Fig. 5b). The shortest lifetime component of 0.8 ns having a relative contribution of 38% is proposed to originate from the surface-related bromine vacancy as discussed earlier (Table S3 of the ESI†).[24,25] The 3.4 ns and 8.1 ns components signify the excitonic recombination process and the surface trap-assisted recombination processes, respectively.24,25 The post-synthetic treatment with OAmBr further amplifies the PLQY to 94% (Fig. S14 of the ESI†). The PL transient of the treated NPLs shows 22% of the fast component. The reduction of the relative percentage of the fast component in treated NPLs is due to the suppression of the bromide vacancy (Table S3 of the ESI†). The PXRD pattern of CPB-2D NPL shows the most prominent lower angle diffraction peak at 3.62° with 5.41°, 7.23°, and 9.01° peaks originating from the (00l) reflection having a periodicity around 1.81° (Fig. 5c–e). This lower angle diffraction is the characteristic signature of the regular stacking pattern in a RP NPL structure.[38–41] To have an idea about the distance of these stacked NPLs, small angle X-ray scattering (SAXS) has been performed (Fig. 5e) where the first diffraction peak is found to originate at 1.83°. From this the inter planner distance of the stacked NPLs were calculated to be 4.9 nm. Considering the chain length of the oleylammonium ion is 1.9 nm and the thickness of the three lead bromide octahedral ($PbBr_6^{4-}$) units is 1.8 nm, the interplanar spacing could be between 3.8 nm (fully stacked condition of spacer cations) and 5.6 nm (head-to-head orientation of spacer cations).[38,39] Therefore, we believe that the interdigitation and locking of the spacer cations between two inorganic layers is less effective in nature, which lengthens the interlayer distance. The schematic representation of the CPB-2D (n = 3) is depicted in Fig. 5f. Also, the PXRD pattern shows characteristic peaks at 15.1° and 30.3°, which correspond to the (100) and (200) planes (marked with a star in Fig. 5c), which are expected in the quasi-2D RP NPL structure, where small 3D $CsPbBr_3$ parts are separated by spacer oleylammonium cations.[38,39] Fig. 5g–i shows the TEM image of the synthesized CPB-2D NPLs. The formation of large

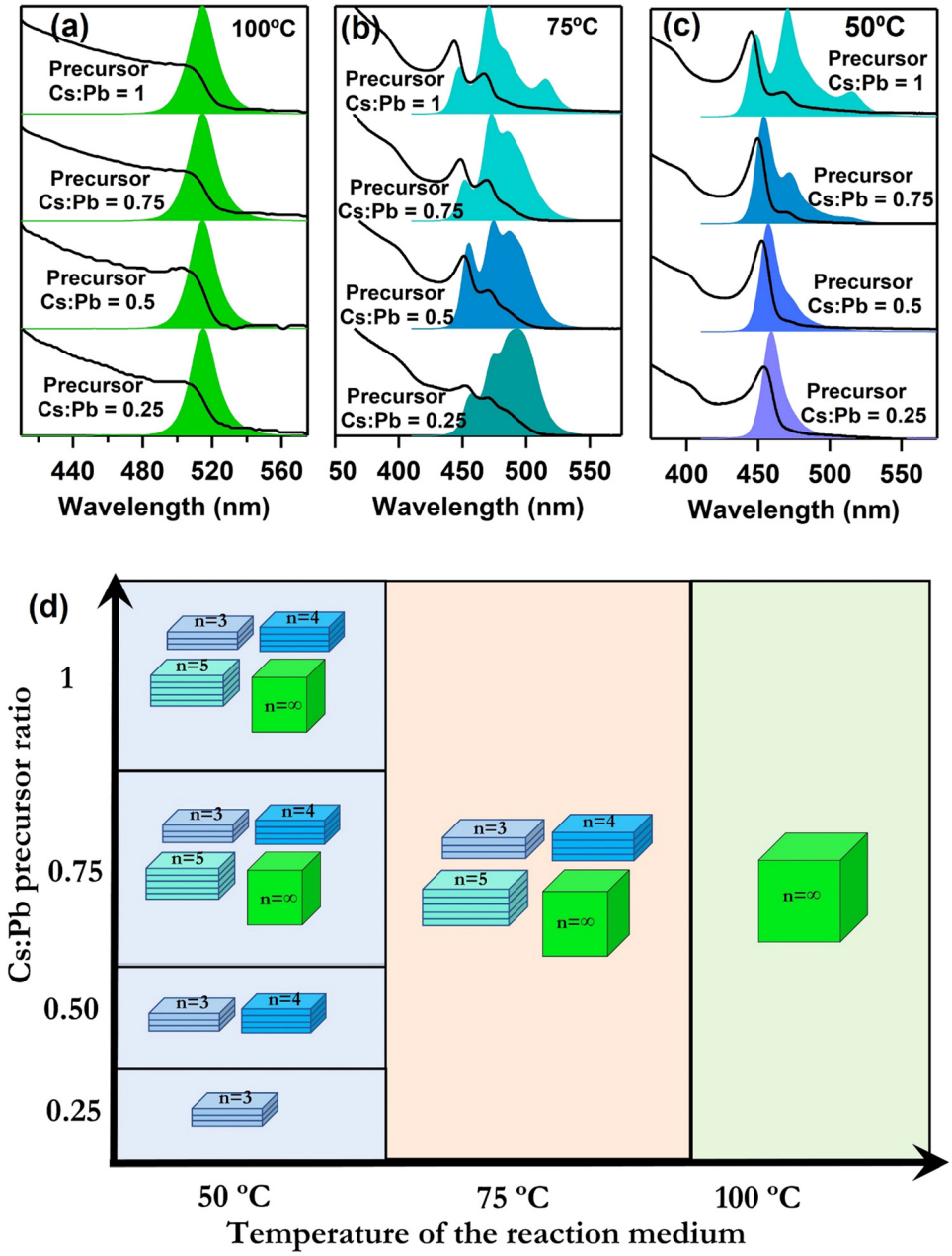

Fig. 4 Effect of cesium to lead precursor (Cs:Pb) ratio (1 to 0.25 from top to bottom) on absorption and PL properties of $CsPbBr_3$ NCs synthesized in a LAMe DES medium (CPB-LAMe) for three different reaction temperatures (a)100 °C (b) 75 °C (c) 50 °C. (d) Schematic representation for the formation of $CsPbBr_3$ NPLs/NC having different thicknesses as a function of temperature and cesium to lead precursor ratio.

2D NPLs can be observed with a lateral dimension in the order of 200 nm. The single crystalline pattern of the NPLs can be seen from the SAED pattern (Fig. S15 of the ESI†). A careful analysis of the TEM results reveals that along with these large nanosheets small ultrathin nanosheets of different shapes are also present. The different contrast in TEM images may be due to formation of a RP type of structure, where different numbers of 2D nanosheets are stacked together. The composition of the NPLs were investigated through the XPS study (Fig. S16 of the ESI†). The RP quasi 2D NPLs have a general formula of $(A')_2A_{n-1}Pb_nX_{3n+1}$ where A′ is the long chain ammonium cation (here Oam^+), A is the A-site cation (here Cs^+) and X is the halide ion (here Br^-). For NPLs with $n = 3$, the structural formula of the system in the present case would be $(OAm)_2Cs_2Pb_3Br_{10}$. The XPS elemental study confirms that the lead to cesium ratio is 1.5, which further suggests the formation of CPB-2D where $n = 3$. The ambient stability of the NPLs was found to be ~2 days through steady-state PL measurements, after which it gradually transforms to a bulk 3D perovskite structure (Fig. S17 of the ESI†).

The results of how temperature affects the product as a whole is a little surprising. Normal hot injection synthesis

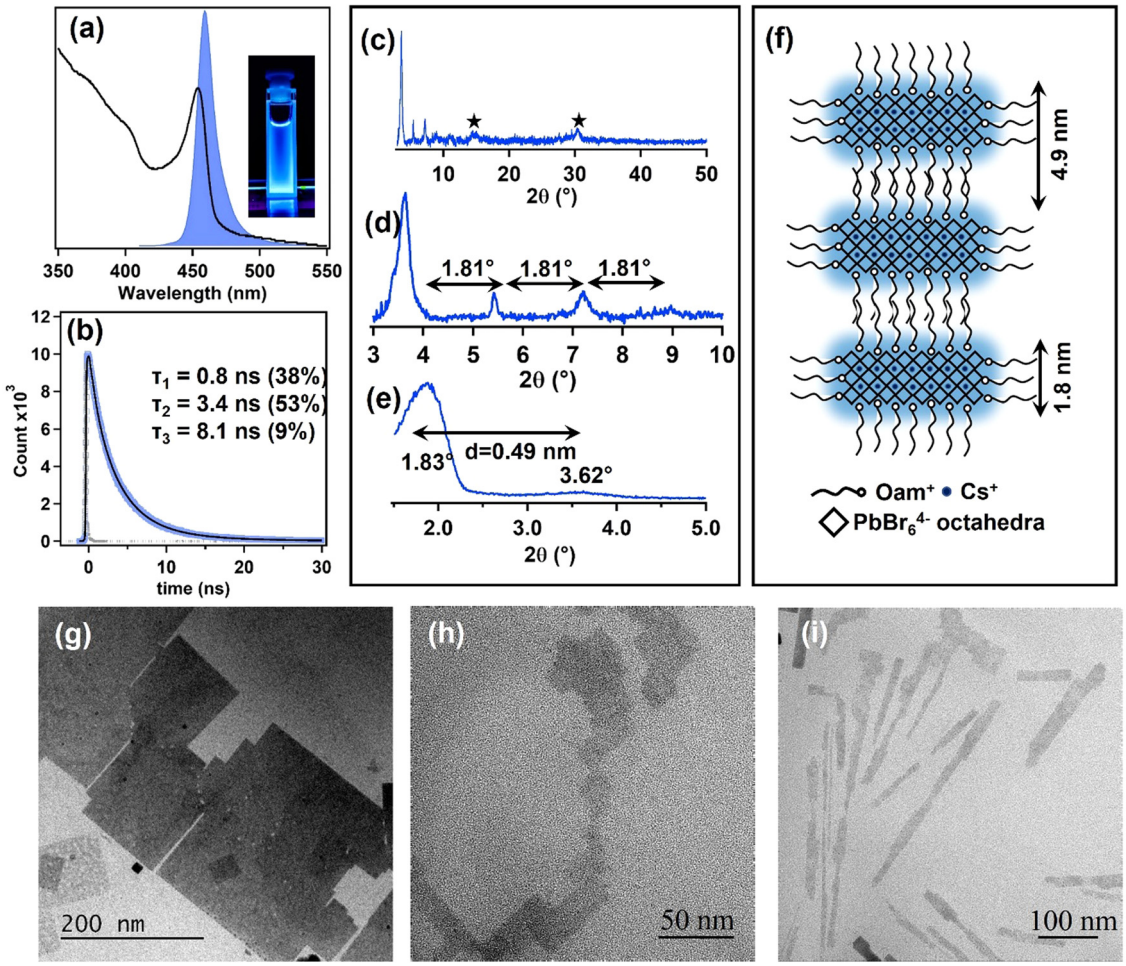

Fig. 5 (a) Absorption and PL of CPB-2D (n = 3). A photograph of CPB-2D under UV light illumination is provided in the inset. (b) Time-resolved PL of a hexane suspension of CPB-2D (n = 3). The excitation wavelength is 405 nm and the instrument response function of the setup is 120 ps. (c) PXRD pattern of CPB-2D (n = 3). (d) Zoomed in version of Fig. 5c at a lower diffraction angle. (e) SAXS pattern of CPB-2D (n = 3). (f) Pictorial representation of RP $(OAm)_2Cs_2Pb_3Br_{10}$ (n = 3) structure. (g–i) TEM images of CPB-2D (n = 3).

favors the formation of larger NCs at high reaction temperatures and is often used for the size-dependent synthesis of $CsPbX_3$ NCs.[30] But in the studied DES medium, unlike the hot injection synthesis process, by lowering the temperature, we ended up with lower-order NPLs of the RP phase. This may be because of the lower solubility of the $PbBr_2$ than OAm in DES medium at lower temperatures, which leads to the formation of the RP structure. To learn more, the reaction pathway needs to be studied in depth in the future.

To check the universality of the DES media for perovskite NC synthesis, we have prepared the chlorine and iodine analogues as well. The PXRD peaks move gradually to the lower diffraction angle from the $CsPbCl_3$ to the $CsPbI_3$ system due to the larger lattice parameter (Fig. S18 of the ESI†), which is consistent with previous studies.[20,42] The band edge absorption shifted to longer wavelengths from $CsPbCl_3$ to $CsPbI_3$ and the PL is also shifted from the violet (pure NCs, PL maxima 413 nm) to the red region (pure NCs, PL maxima 686 nm) (see Fig. 6a–c). The PL transients of all the NCs show the presence of three distinct kinetics (Fig. 6d and Table S4 of the ESI†). The average lifetime gradually increases from 3.9 ns to 21.8 ns from $CsPbCl_3$ NCs to $CsPb(Br/I)_3$ NCs, which is in line with previous reports.[20] However, the average lifetime of $CsPbI_3$ NCs drops drastically and may be due to the presence of large nonradiative decay channels through the trapping sites. A closer look at the PL decay kinetics reveals that in $CsPbCl_3$ NCs the recombination of the charge carriers through the chloride vacancy sites is maximum and also shows very fast decay kinetics (0.3 ns, 80%). The presence of the chloride vacancy is also very common, which restricts its high PLQY in $CsPbCl_3$ NCs.[43] In the present study we estimated the PLQY of $CsPbCl_3$ NCs to be 23%. Going from $CsPbCl_3$ NCs to $CsPb(Br/I)_3$ NCs, the percentage of carrier recombination through the halide vacancy sites decreases, and consequently the PLQY increases (PLQY estimated as 45% and 76% for $CsPb(Cl/Br)_3$ and $CsPb(Br/I)_3$ NCs, respectively). This study further suggests that the involvement of halide vacancies is one of the most important parameters to control the PLQY of the system.

The morphologies of the synthesized NCs were further investigated through TEM. The TEM image of $CsPbCl_3$ suggests

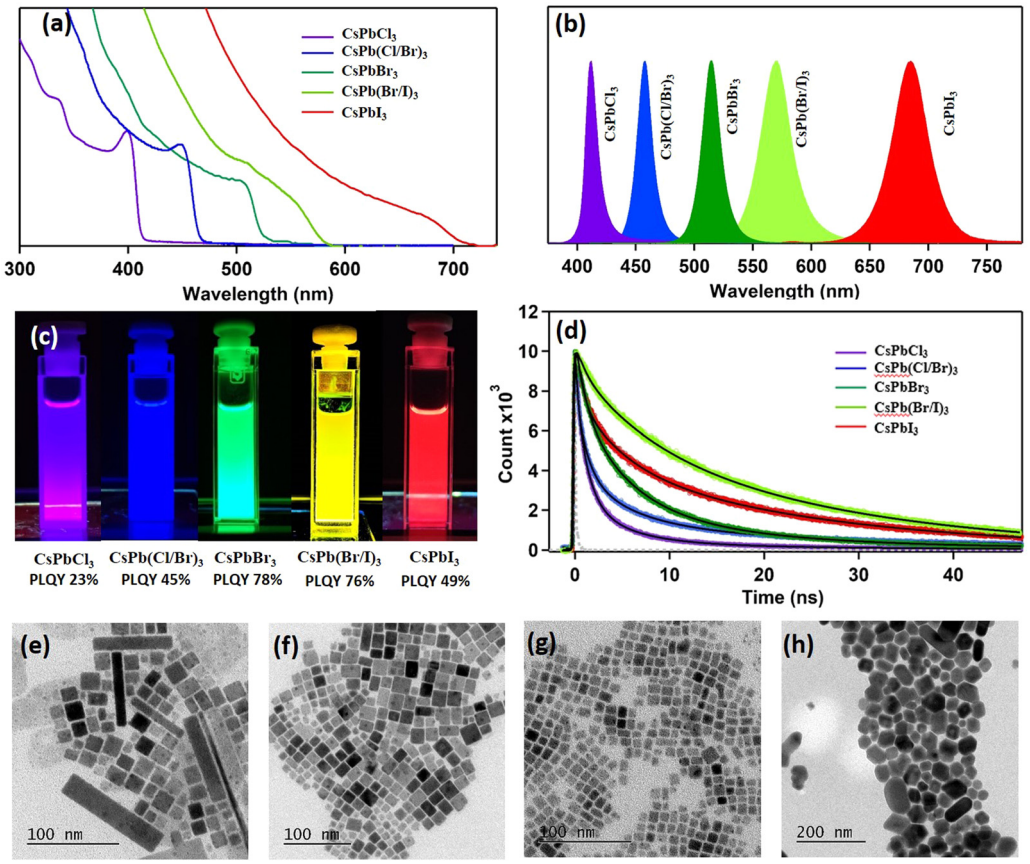

Fig. 6 (a) Absorption spectra (b) PL spectra of $CsPbCl_3$, $CsPb(Cl/Br)_3$, $CsPbBr_3$, $CsPb(Br/I)_3$, and $CsPbI_3$ NCs synthesized in LAMe. (c) Photographic images of $CsPbCl_3$, $CsPb(Cl/Br)_3$, $CsPbBr_3$, $CsPb(Br/I)_3$, and $CsPbI_3$ NCs under UV light synthesized in LAMe. (d) Time-resolved PL spectra of $CsPbCl_3$, $CsPb(Cl/Br)_3$, $CsPbBr_3$, $CsPb(Br/I)_3$, and $CsPbI_3$ NCs synthesized in LAMe. TEM images of (e) $CsPbCl_3$ NCs (f) $CsPb(Cl/Br)_3$ NCs. (g) $CsPb(Br/I)_3$ NCs. (h) $CsPbI_3$ NCs.

the formation of square-shaped NCs along with the formation of some long NPLs types of structure (Fig. 6e). The square-shaped NCs show an average size of 14 ± 8 nm (Fig. S19a of the ESI†). Both $CsPb(Cl/Br)_3$ and $CsPb(Br/I)_3$ show square shaped NC morphology (Fig. 6f and g, respectively) with an average size of 15 ± 7 nm (Fig. S19b of the ESI†) and 9 ± 4 nm (Fig. S19c of the ESI†), respectively. The $CsPbI_3$ shows a unique hexagonal morphology (Fig. 6h) of an average corner distance around 50 ± 20 nm (Fig. S19d of the ESI†) along with a few rod-like shapes. Understanding the mechanism of formation for this hexagonal morphology of $CsPbI_3$ in DES media needs further study.

Conclusion

In conclusion, we have successfully synthesized and characterized all inorganic $CsPbX_3$ perovskite NCs as well as two-dimensional (2D) Ruddlesden–Popper perovskite NPLs ($n = 3$) in environmentally-friendly DES for the first time. The reaction temperature and added precursor ratio have a significant impact on the formation of the NCs with controlled dimensionality. The common surface halide vacancy related defect lowers the PLQY of the synthesized NCs and NPLs, which was restored by oleylammonium halide treatment. The charge carrier dynamics of the synthesized NCs in DES was similar to those of NCs prepared by a regular hot injection procedure. With green DES as a synthesizing medium, our synthesis protocol lowered the crystallization temperature, took place in open atmospheric conditions, and produces good quality NCs with almost uniform size distribution. Our findings indicate that precise control of the chemical environment of the perovskite precursor solution is crucial for producing highly reproducible and efficient NCs, and it opens up a new route for accomplishing this by employing a DES medium.

Conflicts of interest

Authors declare no conflict of interest.

Acknowledgements

S. C. and A. S. acknowledge the IIT Kanpur for providing fellowships. PS thanks the IIT Kanpur for infrastructure and financial support. The authors deeply acknowledge Mr Ashish Kr. Tiwari of the Advanced Centre for Material Science (ACMS),

IIT Kanpur for his continuous help. The authors also thank Mr Jai Kumar Singh of the Advanced Imaging Centre, IIT Kanpur for his help to collect the TEM images. PS thanks the Indian Institute of Technology Kanpur for infrastructure and support.

References

1 C. Capello, U. Fischer and K. Hungerbühler, What is a green solvent? A comprehensive framework for the environmental assessment of solvents, *Green Chem.*, 2007, **9**, 927–934.
2 N. Winterton, The green solvent: a critical perspective, *Clean Technol. Environ. Policy*, 2021, **23**, 2499–2522.
3 E. L. Smith, A. P. Abbott and K. S. Ryder, Deep Eutectic Solvents (DESs) and Their Applications, *Chem. Rev.*, 2014, **114**, 11060–11082.
4 Q. Zhang, K. De Oliveira Vigier, S. Royer and F. Jérôme, Deep eutectic solvents: syntheses, properties and applications, *Chem. Soc. Rev.*, 2012, **41**, 7108–7146.
5 B. B. Hansen, S. Spittle, B. Chen, D. Poe, Y. Zhang, J. M. Klein, A. Horton, L. Adhikari, T. Zelovich, B. W. Doherty, B. Gurkan, E. J. Maginn, A. Ragauskas, M. Dadmun, T. A. Zawodzinski, G. A. Baker, M. E. Tuckerman, R. F. Savinell and J. R. Sangoro, Deep Eutectic Solvents: A Review of Fundamentals and Applications, *Chem. Rev.*, 2021, **121**, 1232–1285.
6 A. Dey, J. Ye, A. De, E. Debroye, S. K. Ha, E. Bladt, A. S. Kshirsagar, Z. Wang, J. Yin, Y. Wang, L. N. Quan, F. Yan, M. Gao, X. Li, J. Shamsi, T. Debnath, M. Cao, M. A. Scheel, S. Kumar, J. A. Steele, M. Gerhard, L. Chouhan, K. Xu, X.-G. Wu, Y. Li, Y. Zhang, A. Dutta, C. Han, I. Vincon, A. L. Rogach, A. Nag, A. Samanta, B. A. Korgel, C.-J. Shih, D. R. Gamelin, D. H. Son, H. Zeng, H. Zhong, H. Sun, H. V. Demir, I. G. Scheblykin, I. Mora-Seró, J. K. Stolarczyk, J. Z. Zhang, J. Feldmann, J. Hofkens, J. M. Luther, J. Pérez-Prieto, L. Li, L. Manna, M. I. Bodnarchuk, M. V. Kovalenko, M. B. J. Roeffaers, N. Pradhan, O. F. Mohammed, O. M. Bakr, P. Yang, P. Müller-Buschbaum, P. V. Kamat, Q. Bao, Q. Zhang, R. Krahne, R. E. Galian, S. D. Stranks, S. Bals, V. Biju, W. A. Tisdale, Y. Yan, R. L. Z. Hoye and L. Polavarapu, State of the Art and Prospects for Halide Perovskite Nanocrystals, *ACS Nano*, 2021, **15**, 10775–10981.
7 M. V. Kovalenko, L. Protesescu and M. I. Bodnarchuk, Properties and potential optoelectronic applications of lead halide perovskite nanocrystals, *Science*, 2017, **358**, 745–750.
8 S. Chen, Y. Zhang, X. Zhang, J. Zhao, Z. Zhao, X. Su, Z. Hua, J. Zhang, J. Cao, J. Feng, X. Wang, X. Li, J. Qi, J. Li and P. Gao, General Decomposition Pathway of Organic–Inorganic Hybrid Perovskites through an Intermediate Superstructure and its Suppression Mechanism, *Adv. Mater.*, 2020, **32**, 2001107.
9 C. C. Boyd, R. Cheacharoen, T. Leijtens and M. D. McGehee, Understanding Degradation Mechanisms and Improving Stability of Perovskite Photovoltaics, *Chem. Rev.*, 2019, **119**, 3418–3451.
10 Z. Xiao, Z. Song and Y. Yan, From Lead Halide Perovskites to Lead-Free Metal Halide Perovskites and Perovskite Derivatives, *Adv. Mater.*, 2019, **31**, 1803792.
11 Q. Fan, G. V. Biesold-McGee, J. Ma, Q. Xu, S. Pan, J. Peng and Z. Lin, Lead-Free Halide Perovskite Nanocrystals: Crystal Structures, Synthesis, Stabilities, and Optical Properties, *Angew. Chem., Int. Ed.*, 2020, **59**, 1030–1046.
12 H.-S. Kim, Y.-J. An, J. I. Kwak, H. J. Kim, H. S. Jung and N.-G. Park, Sustainable Green Process for Environmentally Viable Perovskite Solar Cells, *ACS Energy Lett.*, 2022, **7**, 1154–1177.
13 F. Zhang, S. Huang, P. Wang, X. Chen, S. Zhao, Y. Dong and H. Zhong, Colloidal Synthesis of Air-Stable $CH_3NH_3PbI_3$ Quantum Dots by Gaining Chemical Insight into the Solvent Effects, *Chem. Mater.*, 2017, **29**, 3793–3799.
14 D. T. Moore, K. W. Tan, H. Sai, K. P. Barteau, U. Wiesner and L. A. Estroff, Direct Crystallization Route to Methylammonium Lead Iodide Perovskite from an Ionic Liquid, *Chem. Mater.*, 2015, **27**, 3197–3199.
15 M. T. Hoang, F. Ünlü, W. Martens, J. Bell, S. Mathur and H. Wang, Towards the environmentally friendly solution processing of metal halide perovskite technology, *Green Chem.*, 2021, **23**, 5302–5336.
16 M. T. Hoang, N. D. Pham, Y. Yang, V. T. Tiong, C. Zhang, K. Gui, H. Chen, J. Chang, J. Wang, D. Golberg, J. Bell and H. Wang, A facile, environmentally friendly synthesis of strong photo-emissive methylammonium lead bromide perovskite nanocrystals enabled by ionic liquids, *Green Chem.*, 2020, **22**, 3433–3440.
17 S. Chatterjee, T. Khan, A. Sen, N. Das and P. Sen, Massive amplification of photoluminescence and exceptional water stability of $MAPbBr_3$ nanocrystals through core–shell nanostructure formation in a self-defence mechanism, *Mater. Adv.*, 2022, **3**, 7360–7369.
18 T. Fan, Z. Yan, C. Yang, S. Qiu, X. Peng, J. Zhang, L. Hu and L. Chen, Preparation of menthol-based hydrophobic deep eutectic solvents for the extraction of triphenylmethane dyes: quantitative properties and extraction mechanism, *Analyst*, 2021, **146**, 1996–2008.
19 N. Subba, N. Das and P. Sen, Partial Viscosity Decoupling of Solute Solvation, Rotation, and Translation Dynamics in Lauric Acid/Menthol Deep Eutectic Solvent: Modulation of Dynamic Heterogeneity with Length Scale, *J. Phys. Chem. B*, 2020, **124**, 6875–6884.
20 L. Protesescu, S. Yakunin, M. I. Bodnarchuk, F. Krieg, R. Caputo, C. H. Hendon, R. X. Yang, A. Walsh and M. V. Kovalenko, Nanocrystals of Cesium Lead Halide Perovskites (CsPbX3, X = Cl, Br, and I): Novel Optoelectronic Materials Showing Bright Emission with Wide Color Gamut, *Nano Lett.*, 2015, **15**, 3692–3696.
21 S. Mourdikoudis, M. Menelaou, N. Fiuza-Maneiro, G. Zheng, S. Wei, J. Pérez-Juste, L. Polavarapu and Z. Sofer, Oleic acid/oleylamine ligand pair: a versatile combination in the synthesis of colloidal nanoparticles, *Nanoscale Horiz.*, 2022, **7**, 941–1015.
22 M. Imran, V. Caligiuri, M. Wang, L. Goldoni, M. Prato, R. Krahne, L. De Trizio and L. Manna, Benzoyl Halides as Alternative Precursors for the Colloidal Synthesis of

Lead-Based Halide Perovskite Nanocrystals, *J. Am. Chem. Soc.*, 2018, **140**, 2656–2664.
23 S. Paul and A. Samanta, N-Bromosuccinimide as Bromide Precursor for Direct Synthesis of Stable and Highly Luminescent Green-Emitting Perovskite Nanocrystals, *ACS Energy Lett.*, 2020, **5**, 64–69.
24 T. Ahmed, S. Seth and A. Samanta, Boosting the Photoluminescence of $CsPbX_3$ (X = Cl, Br, I) Perovskite Nanocrystals Covering a Wide Wavelength Range by Postsynthetic Treatment with Tetrafluoroborate Salts, *Chem. Mater.*, 2018, **30**, 3633–3637.
25 S. Chatterjee, M. Ghosal, K. Tiwari and P. Sen, Potassium-Induced Passivation of Deep Traps in Bismuth-Doped Hybrid Lead Bromide Perovskite Nanocrystals: Massive Amplification of Photoluminescence Quantum Yield, *J. Phys. Chem. Lett.*, 2021, **12**, 546–551.
26 S. Chatterjee, P. Dey, N. Das, K. Tiwari, T. Maiti and P. Sen, Reversible Ultra-Slow Crystal Growth of Mixed Lead Bismuth Perovskite Nanocrystals: The Presence of Dynamic Capping, *Chem. – Eur. J.*, 2020, **26**, 1506–1510.
27 F. Zheng, X. Wen, T. Bu, S. Chen, J. Yang, W. Chen, F. Huang, Y. Cheng and B. Jia, Slow Response of Carrier Dynamics in Perovskite Interface upon Illumination, *ACS Appl. Mater. Interfaces*, 2018, **10**, 31452–31461.
28 F. Zheng, W. Chen, T. Bu, K. P. Ghiggino, F. Huang, Y. Cheng, P. Tapping, T. W. Kee, B. Jia and X. Wen, Triggering the Passivation Effect of Potassium Doping in Mixed-Cation Mixed-Halide Perovskite by Light Illumination, *Adv. Energy Mater.*, 2019, **9**, 1901016.
29 M. A. Becker, C. Bernasconi, M. I. Bodnarchuk, G. Rainò, M. V. Kovalenko, D. J. Norris, R. F. Mahrt and T. Stöferle, Unraveling the Origin of the Long Fluorescence Decay Component of Cesium Lead Halide Perovskite Nanocrystals, *ACS Nano*, 2020, **14**, 14939–14946.
30 A. De, N. Mondal and A. Samanta, Hole Transfer Dynamics from Photoexcited Cesium Lead Halide Perovskite Nanocrystals: 1-Aminopyrene as Hole Acceptor, *J. Phys. Chem. C*, 2018, **122**, 13617–13623.
31 N. Mondal and A. Samanta, Complete ultrafast charge carrier dynamics in photo-excited all-inorganic perovskite nanocrystals ($CsPbX_3$), *Nanoscale*, 2017, **9**, 1878–1885.
32 P. Zeng, X. Ren, L. Wei, H. Zhao, X. Liu, X. Zhang, Y. Xu, L. Yan, K. Boldt, T. A. Smith and M. Liu, Control of Hot Carrier Relaxation in $CsPbBr_3$ Nanocrystals Using Damping Ligands, *Angew. Chem., Int. Ed.*, 2022, **61**, e202111443.
33 J. Fu, Q. Xu, G. Han, B. Wu, C. H. A. Huan, M. L. Leek and T. C. Sum, Hot carrier cooling mechanisms in halide perovskites, *Nat. Commun.*, 2017, **8**, 1300.
34 B. Yu, L. Chen, Z. Qu, C. Zhang, Z. Qin, X. Wang and M. Xiao, Size-Dependent Hot Carrier Dynamics in Perovskite Nanocrystals Revealed by Two-Dimensional Electronic Spectroscopy, *J. Phys. Chem. Lett.*, 2021, **12**, 238–244.
35 S. K. Dutta, L. Peng, B. Hudait, R. Xie and N. Pradhan, Halide Perovskite Cluster Precursors: A Paradigm for Obtaining Structure- and Color-Tunable Light-Emitting Nanocrystals, *ACS Energy Lett.*, 2022, **7**, 3177–3186.
36 C. Otero-Martínez, D. García-Lojo, I. Pastoriza-Santos, J. Pérez-Juste and L. Polavarapu, Dimensionality Control of Inorganic and Hybrid Perovskite Nanocrystals by Reaction Temperature: From No-Confinement to 3D and 1D Quantum Confinement, *Angew. Chem., Int. Ed.*, 2021, **60**, 26677–26684.
37 S. Paul, T. Ahmed, S. Das and A. Samanta, Effect of Lead:Halide Precursor Ratio on the Photoluminescence and Carrier Dynamics of Violet- and Blue-Emitting Lead Halide Perovskite Nanocrystals, *J. Phys. Chem. C*, 2021, **125**, 23539–23547.
38 M. C. Weidman, M. Seitz, S. D. Stranks and W. A. Tisdale, Highly Tunable Colloidal Perovskite Nanoplatelets through Variable Cation, Metal, and Halide Composition, *ACS Nano*, 2016, **10**, 7830–7839.
39 A. Sen, S. Chatterjee and P. Sen, UV-Assisted Conversion of 2D Ruddlesden–Popper Iodide Perovskite Nanoplates into Stable 3D $MAPbI_3$ Nanorods, *J. Phys. Chem. C*, 2022, **126**, 18057–18066.
40 F. Zheng, C. Zuo, M. Niu, C. Zhou, S. J. Bradley, C. R. Hall, W. Xu, X. Wen, X. Hao, M. Gao, T. A. Smith and K. P. Ghiggino, Revealing the Role of Methylammonium Chloride for Improving the Performance of 2D Perovskite Solar Cells, *ACS Appl. Mater. Interfaces*, 2020, **12**, 25980–25990.
41 F. Zheng, T. Raeber, S. Rubanov, C. Lee, A. Seeber, C. Hall, T. A. Smith, M. Gao, D. Angmo and K. P. Ghiggino, Spontaneous Formation of a Ligand-Based 2D Capping Layer on the Surface of Quasi-2D Perovskite Films, *ACS Appl. Mater. Interfaces*, 2022, **14**, 51910–51920.
42 P. Bansal, Y. Khan and P. Kar, High luminescence color gradient by physical mixing of two perovskite nanocrystals, *New J. Chem.*, 2019, **43**, 4116–4122.
43 Z.-J. Yong, S.-Q. Guo, J.-P. Ma, J.-Y. Zhang, Z.-Y. Li, Y.-M. Chen, B.-B. Zhang, Y. Zhou, J. Shu, J.-L. Gu, L.-R. Zheng, O. M. Bakr and H.-T. Sun, Doping-Enhanced Short-Range Order of Perovskite Nanocrystals for Near-Unity Violet Luminescence Quantum Yield, *J. Am. Chem. Soc.*, 2018, **140**, 9942–9951.

